Journal of Heat and Mass Transfer Research

Journal homepage: https://jhmtr.semnan.ac.ir

Semnan University

ISSN: 2383-3068

Research Article

Improving the Performance of Liquid-Based Battery Thermal Management Systems Using Flow Patterns and Contact Surface with the Battery

Abolfazl Mokhtari *

Department of Flight and Engineering, Imam Ali University, Tehran, Iran

ARTICLE INFO

Article history:

Received: 2024-08-16

Revised: 2024-09-14

Accepted: 2024-11-20

Keywords:

Electric vehicles;
Thermal management;
Lithium-ion batteries;
Flow pattern;
Solid block.

ABSTRACT

The advancement and commercialization of electric vehicles due to their advantages have increased research in this field. Lithium-ion batteries are among the most important components of electric vehicles, and their performance is affected by temperature. In this study, fluid dynamics and heat transfer in a cooling system for battery cells were investigated using three-dimensional solid-fluid simulations. The thermophysical properties of the cooling fluid were considered variable with temperature and implemented using a user-defined function (UDF). Numerical simulation can effectively predict the thermal behavior of battery cells during discharge and match experimental data. This study examined the impact of different flow patterns and solid block contact surfaces on the maximum surface temperature and temperature distribution uniformity. The results show that the structure of incremental blocks can affect the temperature distribution of battery cells, such that in parallel flow, the maximum temperature of cells near the inlet increases by 0.65°C, and cells near the outlet decreases by 0.2°C. In contrast, in counter-flow, the maximum temperature of side cells is higher by 0.25°C. Additionally, the study shows the impact of increased contact surface on system weight, indicating a significant weight reduction of about 28.5% in solid blocks with increased contact surface. This research demonstrates the potential of using numerical simulations to improve the design of thermal management systems in battery cells.

© 2024 The Author(s). Journal of Heat and Mass Transfer Research published by Semnan University Press.
This is an open access article under the CC-BY-NC 4.0 license. (https://creativecommons.org/licenses/by-nc/4.0/)

1. Introduction

In the era of advanced technology, Battery Thermal Management Systems (BTMS) have become a crucial element in enhancing the performance and safety of lithium-ion batteries. These systems help ensure longevity and optimize the efficiency of batteries by managing their temperature and protecting them from the risks associated with excessive heat. Liquid-based thermal management systems have become the preferred method due to their superior efficiency and precise temperature control. These systems use cooling liquids to dissipate heat from the batteries and maintain an ideal temperature range. Among the benefits of these systems are the reduction of peak temperatures and temperature differences between battery cells, which leads to increased safety and efficiency of the batteries [1]. These systems can operate either directly or indirectly, with the primary goal in both cases being to manage battery temperature and prevent incidents caused by overheating. Recent developments in this field have focused on the use of liquid cooling systems within channels,

* **Corresponding author.**
E-mail address: s.abolfazl.mokhtari@aut.ac.ir

Cite this article as:
Mokhtari, A., 2025. Improving the Performance of Liquid-Based Battery Thermal Management Systems Using Flow Patterns and Contact Surface with the Battery. *Journal of Heat and Mass Transfer Research*, 12(1), pp. 165-176.
https://doi.org/10.22075/JHMTR.2024.34947.1593

yielding positive results in improving the thermal efficiency of batteries [2].

Rao and Zhong [3] investigated the cooling efficiency of a cold plate featuring wedge-shaped microchannels for managing the thermal performance of rectangular batteries. This type of cold plate is installed on the sides and front areas of the battery module. The study found that the temperature distribution uniformity on the front surface decreases due to the reduced contact area between the plate and the battery, as well as the battery's low thermal conductivity. However, wedge-shaped channels not only enhance heat dissipation but also improve the uniformity of temperature distribution on the cold plate's surface. Additionally, these channels increase the pressure drop of the cooling fluid due to the narrowing of the flow path. Pan and colleagues [4,5] compared the performance of manifold microchannel heat sinks with traditional microchannel heat sinks in an experimental study. They concluded that manifold microchannels have lower pressure drops and more uniform temperature distribution compared to traditional microchannels. Furthermore, the higher the aspect ratio of the channels, the more uneven the temperature distribution on the battery surface.

The research found that manifold microchannels have lower pressure drops and provide a more uniform temperature distribution than common microchannels. However, channels with higher aspect ratios result in a more inappropriate temperature distribution on the battery surface. Wei et al. [6] conducted an experimental study on the cooling performance of a flat microchannel using R141b refrigerant for a battery module with five cylindrical batteries. Their findings showed that during phase change and boiling, heat transfer improves, and the temperature difference between the cold plate and battery surface decreases. At a mass flow rate of 598 kg/h, the maximum surface temperature is minimized, and battery capacity is maximized compared to other flow rates. The microchannel plates are arranged in parallel and can have two, three, or four rows in different configurations. Increasing the number of rows increases the contact area between the battery and the cold plate, which reduces the maximum surface temperature and the temperature difference between the battery surfaces and the channels at low discharge rates.

In 2022, Zhou et al. [7] introduced an innovative battery thermal management system utilizing microchannels, where the cooling fluid directly contacts the battery surface. Their experimental and simulation data demonstrated that this design notably enhances temperature uniformity and cooling efficiency. They employed a Gaussian process regression algorithm within a Digital Twin virtual model for optimization analysis. The optimized system showed a reduction in the maximum cell temperature difference by 5.05°C and a decrease in the peak temperature by 4.02°C.

Azizi et al. [8] experimentally investigated the thermohydraulic performance of a cylindrical heat sink microchannel with silver-water nanofluid for battery thermal management applications. Their results show that increasing the Reynolds number of the flow has a more positive effect on increasing the heat transfer rate compared to the mass fraction of nanoparticles. The highest thermal performance coefficient is 1.35, obtained at a mass fraction of 0.8 wt%. In this case, the Nusselt number increases by 67.1% compared to the base fluid, and the pressure drop of the nanofluid under optimal conditions is less than 0.2 bar. Jahanbakhshi et al. [9] explored a cooling method for lithium-ion batteries using a heat sink microchannel paired with a corrugated microtube on the sidewall, along with a silver-water/ethylene glycol nanofluid. By integrating microchannels and microtubes in a counter-flow arrangement, they achieved a more even temperature distribution across the battery surface. This counter-flow setup lowered the battery temperature by 2 to 3°C compared to a parallel-flow configuration. In all scenarios, the temperature variation on the battery surface remained under 5°C.

Recent developments in lithium-ion battery thermal management showcase creative approaches to enhancing the thermal and flow efficiency of these systems. Yang et al. [10] introduced a hybrid thermal management system combining mini-channel liquid cooling and air cooling to lower battery temperatures along the cooling flow direction. Meanwhile, Chen et al. [11] presented a novel hybrid system featuring bionic spiral fins coated with phase change materials (PCM) and integrated liquid cooling. Yang et al. [12] presented a BTMS with a honeycomb geometry using a hexagonal cooling plate and bionic mini-channel liquid cooling. Their system can reduce the maximum battery module temperature to below 40°C at ambient temperatures above 30°C. Additionally, Xiong et al. [13] designed a thermal management system with a bionic liquid flow channel heat exchanger with a spider web geometry, which improves the temperature distribution on the battery surface and reduces its maximum temperature.

These studies highlight the critical role of designing and integrating cooling technologies to manage battery temperatures effectively. By utilizing computational fluid dynamics (CFD)

analyses and equivalent circuit models, researchers have explored how different factors—such as water inlet flow rate, the number of tubes and mini-channel coolers, tube spacing, water flow direction, and spacer combinations—impact the thermal performance of mini-channel liquid cooling systems. The results show that increasing the water inlet flow rate reduces the maximum temperature and temperature difference, and integrating air cooling improves the thermal performance of the hybrid system. These studies offer new ways to improve the thermal management of lithium-ion batteries, which can lead to increased battery life and efficiency. Recent advancements in photovoltaic thermal systems aim to enhance efficiency. Antara et al. [14] used computational fluid dynamics (CFD) simulations to study water flow in four channel pipe variations (circular, hexagonal, semi-circular, and square) to cool PV cells. Circular channels were the most efficient, achieving the lowest PV cell temperatures and highest thermal efficiency. Electrical efficiencies were 14.70% (circular), 14.65% (semi-circular), 14.63% (hexagonal), and 14.62% (square), with corresponding thermal efficiencies of 44.18%, 43.90%, 43.64%, and 43.46%. Magar et al. [15] investigated helical cone coils (HCC) for heat transfer and pressure drop. They found that smaller diameters in HCCs enhance heat transfer but increase pressure drop. The study analyzed heat exchangers with varying angles (θ=70°-90° and θ=30°-50°). Results showed that tube side Nusselt numbers and friction factors increased with Reynolds number (Rei). The highest coil hot water pressure drop (ΔPc) was for θ=0° HE, and the highest shell side cold water pressure drop (ΔPs) was for θ=90° SHE. Pressure drops were influenced by angle and flow rates, with θ=90° SHE showing the highest ΔPs for most shell cold water flow rates of 0.1 kg/s.

Li et al. [16] investigated thermal management systems with side cooling plates and end cooling plates. They found that side cooling plates achieve a lower maximum temperature, whereas end cooling plates offer a more uniform temperature distribution. Shin et al. [17] integrated a thermal management system using solid blocks with liquid channels and an air-based system. Their findings suggest that combining liquid and air systems enhances the performance of the thermal management system by improving temperature distribution uniformity, reducing maximum temperature, and lowering energy consumption. Thakur et al. [18] developed three-level solid blocks for managing the thermal performance of cylindrical batteries. Each block contacts three batteries, with fluid flow parallel to the batteries' axial direction. This design reduces the BTMS weight by over 40% and improves temperature uniformity by up to 75%. Shan et al. [19] analyzed three-level and four-level solid blocks with axial fluid flow. The contact surface of the solid block alters the battery arrangement pattern, with three-level blocks having a staggered arrangement and four-level blocks having an aligned arrangement. Their observations indicate that the four-level block performs better thermally, while the three-level block is significantly lighter. Yates et al. [20] compared a thermal management system with a small channel cylinder to a channel-cooled heat sink. In these systems, fluid flows axially in the battery and perpendicularly to the battery's axial direction, respectively. Results show that the small channel cylinder design achieves a maximum temperature about 0.75℃ lower than the channel-cooled heat sink design, with maximum temperature differences of 3.05℃ and 2℃, respectively. Rao et al. [21] demonstrated that increasing the contact surface in solid blocks containing circular fluid channels can improve temperature distribution uniformity and reduce weight compared to solid blocks with a fixed contact surface, although it does not significantly affect the maximum temperature.

This article examines the impact of flow patterns within channels for a liquid-based thermal management system, focusing on various channels and fixed and increasing solid block contact angles. The main innovation of this research lies in improving the uniformity of temperature distribution and reducing the maximum surface temperature of battery cells. Additionally, this study addresses the reduction of the thermal management system's weight and presents new solutions for optimizing thermal performance and weight reduction.

2. Problem Statement

2.1. Physical and Mathematical Models

Every Figure (1) shows a schematic of the computational domain for various cases in terms of contact angle and flow pattern. Figure (2) presents the dimensions of the computational domain from a front view, with details provided in Table (1). It is noteworthy that two consecutive battery cells are spaced 2 mm apart in the x-direction (longitudinal) and 4 mm apart in the z-direction (transverse). Finally, different geometries for the channel cross-sections are presented in Figure (3). The type of batteries used for this study are 18650 cells.

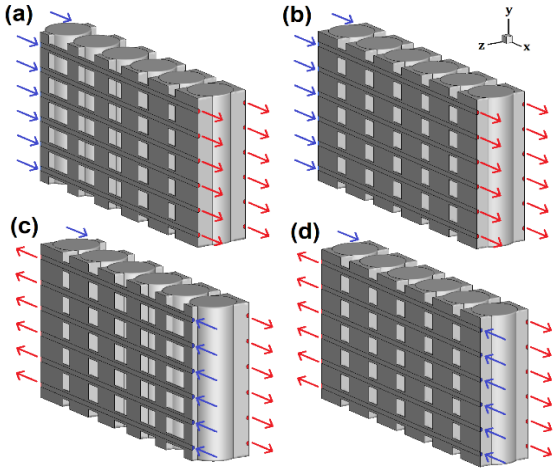

Fig. 1. Schematic of the computational domain: (a) Parallel-flow and incremental blocks, (b) Parallel-flow and fixed blocks, (c) Counter-flow and incremental blocks, (d) Counter-flow and fixed blocks.

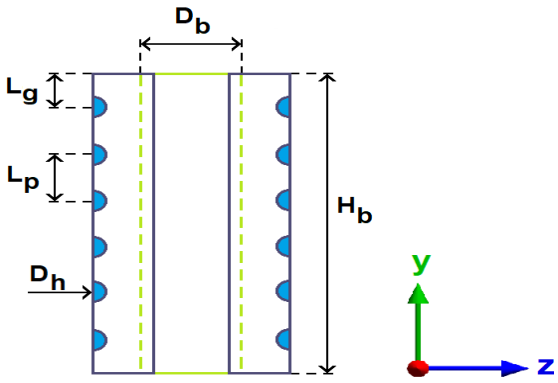

Fig. 2. Dimensions of the computational domain.

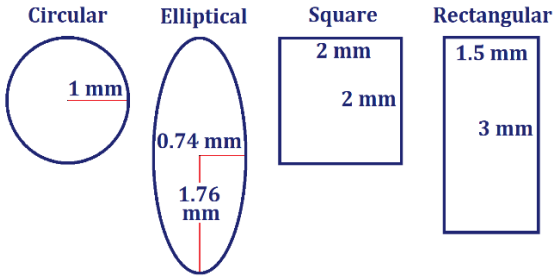

Fig. 3. Various geometries of the channel cross-sections.

Table 1. Dimensions of the computational domain.

Parameter	Symbol (Unit)	Size
Battery Diameter	D_b(mm)	18
Battery Height or Solid Block Height	H_b(mm)	65
Hydraulic Diameter of the Channel	D_h(mm)	2
Center-to-Center Distance of Two Adjacent Channels	L_p(mm)	10.8
Distance from the Edge of the Solid Block to the Center of the First Channel	L_g(mm)	4.5
Width of the Solid Block in Contact with Each Battery	W_s(mm)	14

In the conducted research, fluid dynamics and thermal energy transfer were modeled using a comprehensive three-dimensional solid-fluid simulation. The simulations were performed using ANSYS Fluent software. The fluid behavior is characterized as unidirectional, laminar, incompressible, and steady-state. The thermophysical properties of the coolant fluid vary with temperature and are implemented through a user-defined function (UDF) in the program. The simulation ignores the effects of gravitational forces and heat transfer due to natural convection. Additionally, this study does not account for heat transfer by radiation and thermal resistance at the interface between the solid block and the battery, nor does it exclude viscous dissipation. According to these premises, the flow within the channels is governed by the continuity (1), momentum (2), and energy (5) equations, which are outlined as follows [22]:

$$\vec{\nabla}.\vec{V} = 0 \tag{1}$$

$$\rho\frac{D\vec{V}}{Dt} = -\vec{\nabla}p + \vec{\nabla}.\tau'_{ij} \tag{2}$$

here, the terms τ'_{ij} and $\frac{D\vec{V}}{Dt}$ are expressed as follows:

$$\tau'_{ij} = \mu\left(\frac{\partial u_i}{\partial x_j} + \frac{\partial u_j}{\partial x_i}\right) \tag{3}$$

$$\frac{D\vec{V}}{Dt} = \frac{\partial\vec{V}}{\partial t} + u\frac{\partial\vec{V}}{\partial x} + v\frac{\partial\vec{V}}{\partial y} + w\frac{\partial\vec{V}}{\partial z} \tag{4}$$

$$\rho c_p\frac{DT}{Dt} = \vec{\nabla}.\left(k\vec{\nabla}T\right) \tag{5}$$

In the above equations, the symbols (p), (T), and (u, v, w) correspond to the pressure, temperature, and velocity components, respectively. Additionally, (ρ), (μ), (c_p), and (k) represent the fluid's density, viscosity, specific heat capacity, and thermal conductivity, respectively. The governing energy equation for the solid block is derived as follows:

$$\rho_s C_{p,s}\frac{DT_s}{Dt} = \vec{\nabla}.\left(k_s\vec{\nabla}T_s\right) \tag{6}$$

The energy equation for the battery is defined as follows [23]:

$$\rho_b C_{p,b}\frac{DT_b}{Dt} = \vec{\nabla}.\left(k_b\vec{\nabla}T_b\right) + Q_b \tag{7}$$

The density, specific heat, and thermal conductivity of the aluminum solid block are 2719 $kg.m^{-3}$, 871 $J.kg^{-1}.K^{-1}$, and 202.4 $W.m^{-1}.K^{-1}$, respectively. The density and specific heat of the battery cell are 2317 $kg.m^{-3}$ and 985 $J.kg^{-1}.K^{-1}$, and its thermal conductivity in the axial and radial directions are 32.9 $W.m^{-1}.K^{-1}$ and 3.8 $W.m^{-1}.K^{-1}$, respectively.

In the transient analysis of lithium-ion battery modules, accurately determining the amount of heat generated during the discharge phase (Q_b) is crucial. Two main sources of heat generation in battery cells are recognized in the scientific literature [24]. The first source is irreversible heat (Q_{irr}), caused by the electrical resistance within the cell and commonly known as Joule heating. The second source is reversible heat (Q_{rev}), which is related to the heat generated by electrochemical reactions in the battery.

$$Q_b = Q_{irr} + Q_{rev} \tag{8}$$

$$Q_{irr} = I(E - V) = I^2 R_e \tag{9}$$

$$Q_{rev} = -T\Delta S\left(\frac{I}{nF}\right) = -I^2\left[T\left(\frac{dE}{dT}\right)\right] \tag{10}$$

To precisely assess the total heat produced by a lithium-ion battery, it is crucial to determine the values of (R_e) and ($\frac{dE}{dT}$). The overall internal resistance of the battery is derived using a sophisticated nonlinear curve-fitting approach. Taking into account the battery cell temperature (T) in Kelvin and its state of charge (SOC), which is calculated using the Coulomb counting method, the formula for (R_e) is given as follows [25]:

$$\begin{aligned} R_e = (&-112 \times SOC^3 \\ &- 0.203 \times SOC^2 \times T \\ &+ 0.000737 \times SOC \times T^2 \\ &+ 0.00000753 \times T^3 \\ &+ 301 \times SOC^2 \\ &- 0.144 \times SOC \times T \\ &- 0.0061 \times T^2 \\ &- 188 \times SOC \\ &+ 1.28 \times +23.6) \\ &\times 10^{-3} \end{aligned} \tag{11}$$

The relationship between the entropy coefficient (dE/dT) in lithium-ion batteries is more influenced by the state of charge (SOC). This coefficient can be effectively described as a function of SOC. A specialized equation representing (dE/dT) as a function of SOC is expressed as follows [25]:

$$\begin{aligned} \frac{dE}{dT} = (&-0.342 + 0.979 \times SOC \\ &- 1.49 \times SOC^2 \\ &+ 0.741 \times SOC^3) \\ &\times 10^{-3} \end{aligned} \tag{12}$$

This equation provides an accurate mathematical representation of how the entropy coefficient changes with variations in the battery's SOC. Jiaqiang et al. [25] have shown that heat generation, represented by Q_r, is more related to SOC than time (t). For a constant discharge rate xC, the relationship between t and SOC can be expressed as follows:

$$SOC = 1 - x.t \tag{13}$$

The C-rate represents the battery's charge and discharge current. According to the C-rate equation [26]:

$$C - rate = \frac{\text{Charging or Discharging current (A)}}{\text{Rated battery capacity (Ah)}} \tag{14}$$

In this study, a discharge rate of 3C and a discharge current of 7.8A were considered.

Based on the information obtained from equations (8) to (14), a user-defined function (UDF) has been developed to represent the transient heat generation rate in a battery. This UDF has been successfully incorporated into ANSYS Fluent and acts as a heat source for the battery. The standard method chosen for pressure interpolation is the standard method. For the spatial discretization of the convective equations, the second-order upwind method has been used. Finally, if the residuals from solving the continuity, momentum, and energy equations are less than 10^{-6}, it can be said that the solution has reached the desired accuracy, and the solving process can be concluded. This value is considered the convergence criterion for the solution field. The relationships used to determine the temperature-dependent thermophysical properties of water are as follows [27]:

$$\rho_w = 1000 \times \left[1.0 - \frac{(T_w - 4.0)^2}{119000 + 1365 \times T_w - 4 \times (T_w)^2}\right] \tag{15}$$

$$\begin{aligned} k_w = 0.56112 &+ 0.00193 \times T_w \\ &- 2.60152749e \\ &- 6 \times (T_w)^2 \\ &- 6.08803e \\ &- 8 \times (T_w)^3 \end{aligned} \tag{16}$$

$$\begin{aligned} \mu_w = 0.00169 &- 4.25263e - 5 \times T_w \\ &+ 4.9255e \\ &- 7 \times (T_w)^2 \\ &- 2.09935e \\ &- 9 \times (T_w)^3 \end{aligned} \tag{17}$$

$$\begin{aligned} C_{p,w} = 4217.629 &- 3.20888 \times T_w \\ &+ 0.09503 \times (T_w)^2 \\ &- 0.00132 \times (T_w)^3 \\ &+ 9.415e - 6 \times (T_w)^4 \\ &- 2.5479e \\ &- 8 \times (T_w)^5 \end{aligned} \tag{18}$$

The above relationships are valid for water temperatures (T_w) between 0 and 100℃. The boundary conditions applied in this analysis are detailed below [28]:

At the channel inlets,

$$u = u_{in}, v = 0, w = 0, T = T_{in} = 298.15\text{K} \quad (19)$$

At the channel outlets,

$$p = p_{out} = 1\ atm \quad (20)$$

The following conditions apply at the boundary where the channel wall meets the fluid [29]:

$$u = v = w = 0, T_f = T_s, -k_f\left(\partial T_f/\partial n\right) = -k_s\left(\partial T_s/\partial n\right), h(T_s - T_b) = -k_s\left(\partial T_s/\partial n\right) \quad (21)$$

here, T_b represents the bulk fluid temperature.

2.2. Grid Independence Study and Validation

To guarantee accurate results unaffected by the number of network elements, a grid independence test was performed on the battery thermal management system with parallel flow at a 3C discharge rate. This test was performed on three networks with different numbers of elements, and the results are recorded in Table (2) for rectangular and circular channels. Initially, the simulation started with 634,000 cells. Then, the number of cells was increased to 1,658,000 and 3,850,000. Analysis of the results showed that with an increase in the number of cells from 634,000 to 1,658,000, the maximum temperature changes for rectangular channels were 1.6% and for circular channels were 1.1%. When the number of cells reached 3,850,000, the maximum temperature changes compared to 1,658,000 cells were calculated to be 0.2% for rectangular channels and 0.14% for circular channels. Therefore, considering the accuracy of the results, computation speed, and simulation costs, a network with 1,658,000 cells was selected as the standard network for all simulations.

Table 2. Examination of the independence of results from the number of networks for rectangular and circular channels at a discharge rate of 3C and asymmetric flow.

Number of Networks	Maximum Temperature of Battery Module for Circular Channels (℃)	Error (%)	Maximum Temperature of Battery Module for Rectangular Channels (℃)	Error (%)
634,000	41.87	-	38.62	-
1,658,000	42.35	1.15%	39.25	1.63%
3,850,000	42.41	0.14%	39.33	0.2%

Figure 4 illustrates the comparison between the current numerical simulation and the experimental data from Huang et al. [23] for a battery cell at three different discharge rates. The graph shows the maximum surface temperature of the battery over time, with two lines for each discharge rate: one for the experimental data and one for the numerical simulation data. As observed, at all three discharge rates, the experimental data and numerical simulation data are well aligned. However, the average absolute deviation (A.A.D.%) is lowest at a discharge rate of 1C. Despite the average absolute deviation increasing to 2.3% at a discharge rate of 3C, it is still below the standard error rate (5%). Therefore, this chart indicates that the numerical simulation can effectively predict the thermal behavior of the battery cell during discharge, and this model is valid for simulating battery heat generation. Figure 5 shows a view of the meshing used in this study. The following equation is used to calculate the average absolute deviation (A.A.D.%), which indicates the difference between the experimental data and the numerical results at different discharge rates [30]:

$$\text{A. A. D. \%} = 100 \times \sum_{i=1}^{n}\left|\frac{T_i^{Exp} - T_i^{Num}}{T_i^{Exp}}\right|/n \quad (22)$$

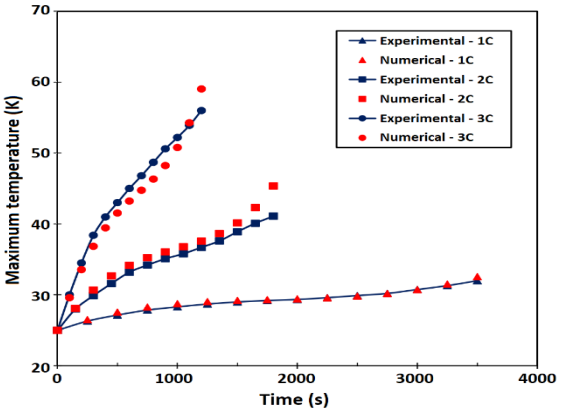

Fig. 4. Validation of the present study with the experimental data of Huang et al. [21].

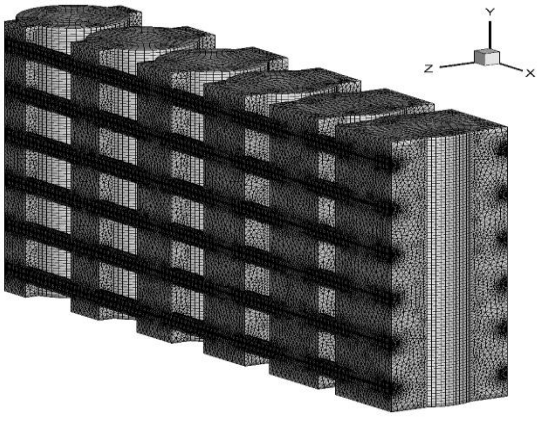

Fig. 5. View of the computational domain meshing.

3. Discussion and Analysis

A numerical simulation was performed to evaluate a liquid-based thermal management system for cylindrical cells. The study focused on the maximum surface temperature and temperature distribution uniformity under different flow patterns, considering both constant and increasing contact surfaces. The findings for various conditions are discussed below.

Figure 6 illustrates the maximum temperature of each cell for scenarios with constant and increasing contact angles. Figure 6a depicts the counterflow pattern, while Figure 6b shows the parallel flow pattern. In the parallel flow configuration, the increasing block structure raises the maximum temperature of the battery cells near the inlet and lowers it for cells near the outlet. This occurs due to the reduced contact surface between the thermal management system and the battery cell at the inlet, which increases as the cells approach the outlet. For instance, in parallel flow with rectangular channels, the maximum temperature of the cell nearest to the inlet rises by 0.65°C, while the maximum temperature of the cell closest to the outlet drops by 0.2°C compared to the constant contact surface scenario. However, the average temperature of the six cells in the computational domain between the increasing and constant surface cases is approximately 0.1°C.

In the counterflow pattern, the maximum temperature of the side cells is higher in the increasing contact surface scenario, while other cells exhibit lower maximum temperatures. This phenomenon is due to the reduced contact surface on both sides of the side cells compared to the constant surface scenario. Considering the flow pattern and contact surface, the thermal and surface balance in the cells is greater in the counterflow case than in the parallel flow case, resulting in a larger temperature difference between the constant and increasing surface scenarios. For example, in rectangular channels, the maximum temperature difference between battery cells ranges from 0.2 to 0.25°C. Additionally, the average maximum temperature difference between the constant and increasing surface scenarios in counterflow is about 0.08°C.

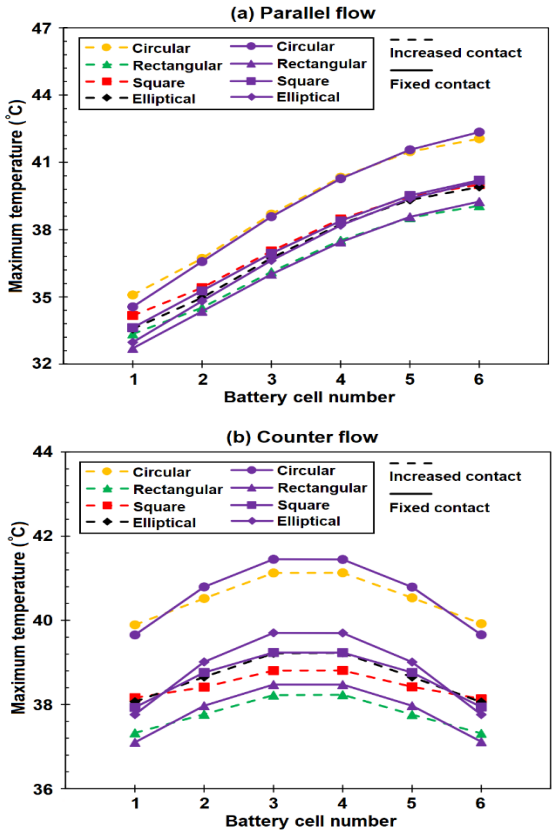

Fig. 6. Maximum temperature for different contact surfaces and flow patterns for battery cells: (a) Parallel-flow, (b) Counter-flow.

Figure 7 illustrates the temperature variations in the battery module across different contact surfaces and flow patterns for various channel cross-sections. It is clear that in parallel flow, the use of solid blocks with larger contact surfaces, as opposed to constant contact surfaces, does not significantly decrease the temperature difference in the battery module. Overall, increasing the contact surfaces tends to yield better performance. However, in parallel flow, in neither the increasing nor constant contact surface cases does the temperature difference of the battery module decrease below 5°C (the safe temperature difference range [31]). On the other hand, for counterflow, using solid blocks with increasing contact surfaces increases the temperature difference of the battery module and reduces the uniformity of the temperature distribution. Only for square channels is this performance maintained, slightly reducing the temperature difference. Despite the increased temperature difference for other channels, the temperature difference remains below 4°C and within the safe range.

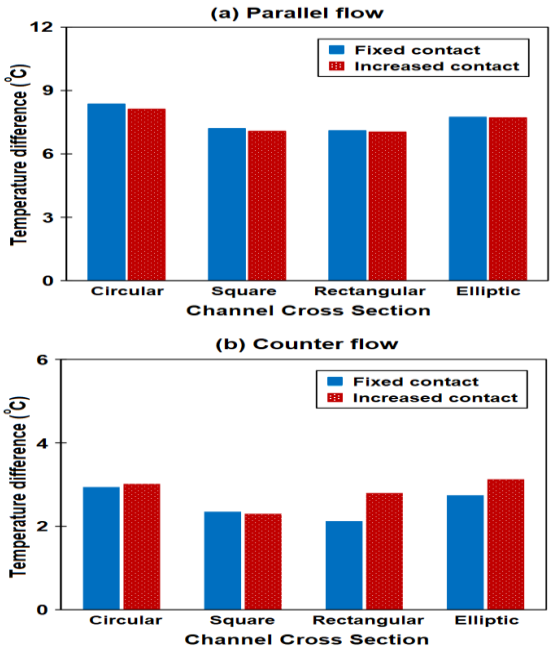

Fig. 7. Temperature difference of the battery module for different contact surfaces and flow patterns for various channel cross-sections: (a) Parallel-flow, (b) Counter-flow.

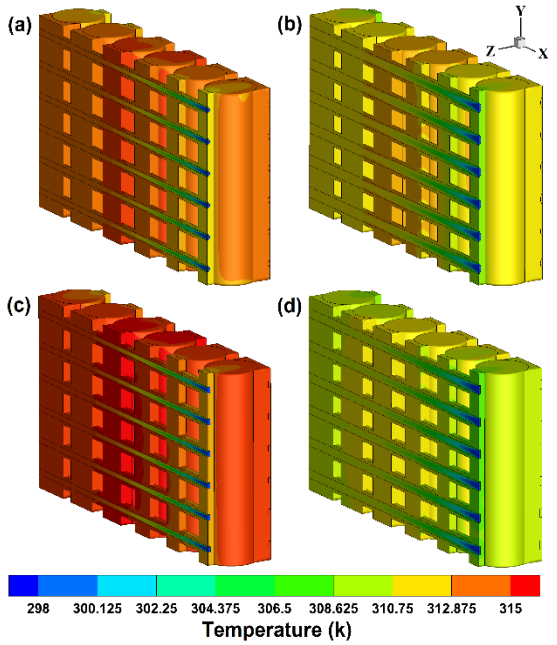

Fig. 9. Temperature contour for counter-flow with increasing contact surface: (a) circular channel, (b) elliptical channel, (c) square channel, and (d) rectangular channel.

Figures 8 and 9 illustrate the temperature contours for both parallel and counterflow configurations with an increasing contact surface. In the parallel flow scenario, the circular channel exhibits the highest maximum temperature, particularly on the cell surface near the channel outlet. Conversely, the rectangular channels display the lowest maximum temperature. The minimum temperature also occurs for rectangular channels on the cell surface near the inlet. For counterflow, the maximum temperature occurs in the middle cells, with the highest temperature recorded by the square channels. This is due to the presence of opposing cooling flow on both sides of the cells. The minimum temperature is also obtained in the side cells for rectangular channels.

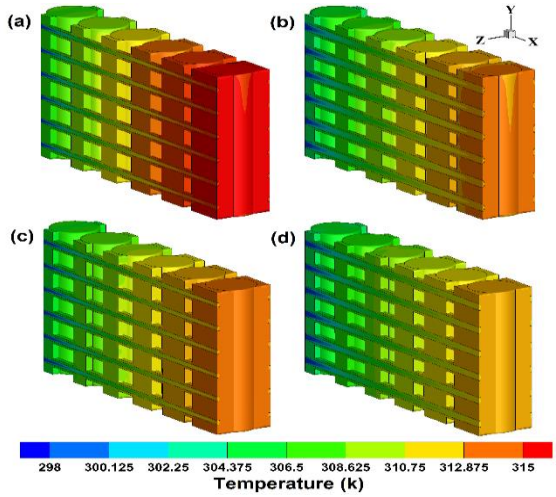

Fig. 8. Temperature contour for parallel-flow with increasing contact surface: (a) circular channel, (b) elliptical channel, (c) square channel, and (d) rectangular channel.

Figure 10 illustrates the pressure drop (in Pascals) for four different channel cross-section shapes: Circular, Square, Rectangular, and Elliptic, with data divided into parallel and counter flow Patterns. For the Circular cross-section, the pressure drop is approximately 73.01 Pa for the parallel flow pattern and 70.74 Pa for the counter flow pattern, showing the minimal difference. The square cross-section shows a pressure drop of about 67.14 Pa for parallel-flow and a significant decrease to 64.67 Pa for counter-flow, indicating higher efficiency in the latter configuration. The rectangular cross-section has a pressure drop of roughly 74.24 Pa for parallel-flow and 71.99 Pa for counter-flow, demonstrating stable performance similar to the circular shape. The elliptic cross-section exhibits the highest pressure drop, with approximately 76.91 Pa for parallel-flow and 75.67 Pa for counter-flow, indicating higher resistance to fluid flow. Overall, the elliptic shape shows the highest pressure drop, while the square shape demonstrates the most significant difference between flow patterns, suggesting potential optimization opportunities. These variations in pressure drop across different shapes and flow patterns are crucial for designing efficient fluid transport systems, providing valuable insights for engineering applications. It can be seen that the pressure drop is lower for the non-uniform flow with the same channel length, hydraulic diameter and cross-sectional area. This phenomenon is due to the fact that the average fluid temperature is higher in non-symmetrical flow than in parallel flow. Since a fluid with a higher temperature has less resistance to flow, its

viscosity is lower, and therefore the pressure drop is reduced.

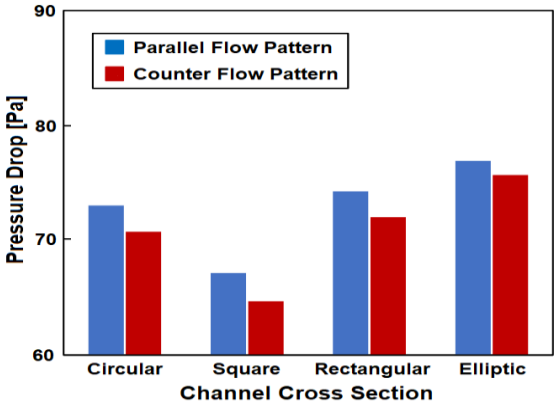

Fig. 10. Pressure Drop Comparison in Different Channel Cross-Section Shapes for Parallel and Counter Flow Patterns.

Figure 11 measures the system weight (computational domain) without considering the battery cells and the flow within the channels. The weight of the solid blocks designed in CATIA software is measured. It is observed that the system weight for solid blocks with increasing contact surfaces is less than for constant contact surfaces. The weight reduction is about 28.5% for solid blocks with square and rectangular channels and about 29% for circular and elliptical channels. It is observed that for the same contact surface, circular and elliptical channels have less weight than rectangular and square channels. For example, in the increasing contact surface case, square and rectangular channels weigh 0.07 kg, while elliptical and circular channels weigh 0.069 kg. The weight difference between the channels is due to differences in their perimeter and area. For example, for circular and square channels with a hydraulic diameter of 2 mm, the cross-sectional area is 3.14 mm^2 and 4 mm^2, respectively. Since channels with the same cross-sectional geometry are designed between the solid blocks, the smaller area of circular and elliptical channels reduces their weight. All numbers are based on the computational domain geometry.

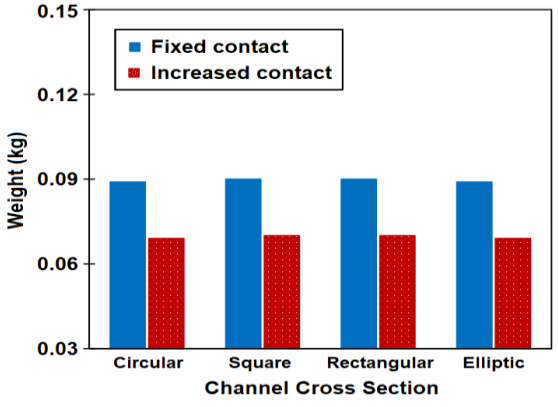

Fig. 11. Weight of solid blocks for different cases.

4. Conclusions

In this research, three-dimensional simulations were employed to examine the fluid dynamics and heat transfer within a liquid-based thermal management system for cylindrical battery cells. The findings revealed that block structures with larger contact surface areas influence the temperature distribution and peak temperature of the battery cells. In a parallel-flow configuration, these structures raise the temperature of cells near the inlet and lower it near the outlet. Conversely, in a counter-flow setup, they increase the maximum temperature of the side cells. The study also demonstrated that variations in contact surface area and flow pattern affect the temperature difference within the batteries. In parallel-flow, a larger contact surface area does not significantly diminish the temperature difference, whereas in counter-flow, it can increase the temperature difference and decrease the uniformity of the temperature distribution. For square channels, this contact surface area somewhat reduces the temperature difference. In parallel-flow with rectangular channels, the maximum temperature of the cell nearest to the inlet rises by 0.65°C, while the maximum temperature of the cell closest to the outlet drops by 0.2°C. In counter-flow, the maximum temperature difference between battery cells ranges from 0.2 to 0.25°C. Also, for all cross-sections, the pressure drop is lower for the counter-flow pattern.

Finally, the simulations showed that the weight of the system for solid blocks with increased contact surface area is less, which can be beneficial for reducing the overall weight of the thermal management system. The weight reduction for solid blocks with increasing contact surfaces is about 28.5% for square and rectangular channels and about 29% for circular and elliptical channels. This weight reduction can help improve the overall performance of the system, as less weight means less energy is required for movement and cooling. In summary, this study demonstrated that the design of the thermal management system and the selection of appropriate contact surface area and flow pattern can have a significant impact on the thermal performance and weight of the system. These findings can be used to optimize thermal management systems in the future.

Nomenclature

BTMS	Battery thermal management system
C_p	Specific heat capacity [$J \cdot kg^{-1} \cdot K^{-1}$]
EV	Electric vehicle

k	Thermal conductivity [W $m^{-1}·K^{-1}$]
P	Pressure [Pa]
PCM	Phase change material
SOC	State of charge
T	Temperature [K]
UDF	User-defined function
Q_b	Heat power produced during the discharge phase [W]
Q_{irr}	Irreversible heat [W]
Q_{rev}	Reversible heat [W]
μ	Viscosity [$kg·m^{-1}·s^{-1}$]
ρ	Density [$kg·m^{-3}$]

Funding Statement

This research did not receive any specific grant from funding agencies in the public, commercial, or not-for-profit sectors.

Conflicts of Interest

The author declares that there is no conflict of interest regarding the publication of this article.

References

[1] Sarvar-Ardeh, S., Rashidi, S., Rafee, R., Karimi, N., 2023. A review on the applications of micro-/mini-channels for battery thermal management. Journal of Thermal Analysis and Calorimetry, 148, pp. 7959-7979. doi: https://doi.org/10.1007/s10973-023-12092-6.

[2] Hwang, F. S., Confrey, T., Reidy, C., Picovici, D., Callaghan, D., Culliton, D., Nolan, C., 2024. Review of battery thermal management systems in electric vehicles. Renewable and Sustainable Energy Reviews, 192, 114171. doi: https://doi.org/10.1016/j.rser.2023.114171.

[3] Rao, Z., Zhang, X., 2019. Investigation on thermal management performance of wedge-shaped microchannels for rectangular Li-ion batteries. Int. J. Energy Research 43, pp. 3876-3890. doi: https://doi.org/10.1002/er.4571.

[4] Pan, M., Zhong, X., Dong, G., Huang, G., 2019. Experimental study of the heat dissipation of battery with a manifold micro-channel heat sink. Applied Thermal Engineering, 163, 114330. doi: https://doi.org/10.1016/j.applthermaleng.2019.114330.

[5] Pan, M., Hu, M., 2020. Numerical Simulation of Manifold Microchannel Heat Sinks for Thermal Management in a Li-Ion Battery. Chemical Engineering & Technology, 43, pp. 2501-2513. doi: https://doi.org/10.1002/ceat.202000316.

[6] Wei, L., Jia, L., An, Z., Dang, C., 2020. Experimental study on thermal management of cylindrical Li-ion battery with flexible microchannel plates. Journal of Thermal Science, 29, pp. 1001–1009. doi: https://doi.org/10.1007/s11630-020-1331-1.

[7] Xu, Z., Xu, J., Guo, Z., Wang, H., Sun, Z., Mei, X., 2020. Design and Optimization of a Novel Microchannel Battery Thermal Management System Based on Digital Twin. Energies, 15, 1421. doi: https://doi.org/10.3390/en15041421.

[8] Azizi, Z., Barzegarian, R., Behvandi, M., 2022. Design-expert aided thermohydraulic assessment of a nanofluid-cooled cylindrical microchannel heat sink: Possible application for thermal management of electric vehicle batteries. Sustainable Energy Technologies and Assessments, 50, 101876. doi: https://doi.org/10.1016/j.seta.2021.101876.

[9] Jahanbakhshi, A., Nadooshan, A.A., Bayareh, M., 2022. Cooling of a lithium-ion battery using microchannel heatsink with wavy microtubes in the presence of nanofluid. J. Energy Storage, 49, 104128. doi: https://doi.org/10.1016/j.est.2022.104128.

[10] Yang, W., Zhou, F., Zhou, H., Wang, Q., Kong, J., 2020. Thermal performance of cylindrical lithium-ion battery thermal management system integrated with mini-channel liquid cooling and air cooling. Applied Thermal Engineering, 175, 115331. doi: https://doi.org/10.1016/j.applthermaleng.2020.115331.

[11] Chen, X., Shen, J., Xu, X., Wang, X., Su, Y., Qian, J., Zhou, F., 2024. Performance of thermal management system for cylindrical battery containing bionic spiral fin wrapped with phase change material and embedded in

liquid cooling plate. Renewable Energy, 223, 120087. doi: https://doi.org/10.1016/j.renene.2024.120087.

[12] Yang, W., Zhou, F., Liu, Y., Xu, S., Chen, X., 2021. Thermal performance of honeycomb-like battery thermal management system with bionic liquid mini-channel and phase change materials for cylindrical lithium-ion battery. Applied Thermal Engineering, 188, 116649. doi: https://doi.org/10.1016/j.applthermaleng.2021.116649.

[13] Xiong, X., Wang, Z., Fan, Y., Wang, H., 2023. Numerical analysis of cylindrical lithium-ion battery thermal management system based on bionic flow channel structure. Thermal Science and Engineering Progress, 42, 101879. doi: https://doi.org/10.1016/j.tsep.2023.101879.

[14] Antara I., Sucipta M., Astawa K., Wirawan I., Sukrawa M., 2024. CFD Simulation of Photovoltaic Thermal (PV/T) Cooling System with Various Channel Geometries. Journal of Heat and Mass Transfer Research. doi: https://doi.org/10.22075/jhmtr.2024.33787.1551.

[15] Magar S.M., Gugliani G.K., Navthar R.R., 2024. Experimental Heat Transfer Analysis of Helical Coiled Tubes on the Basis of Variation in Curvature Ratio and Geometry. Journal of Heat and Mass Transfer Research, 11, 89-108. doi: https://doi.org/10.22075/jhmtr.2024.32179.1491.

[16] Li, L., Ling, L., Xie, Y., Zhou, W., Wang, T., Zhang, L., Bei, S., Zheng, K., Xu, Q., 2023. Comparative study of thermal management systems with different cooling structures for cylindrical battery modules: Side-cooling vs. terminal-cooling. Energy, 274, 127414. doi: https://doi.org/10.1016/j.energy.2023.127414.

[17] Xin, S., Wang, C., Xi, H., 2023, Thermal management scheme and optimization of cylindrical lithium-ion battery pack based on air cooling and liquid cooling. Applied Thermal Engineering, 224, 120100. doi: https://doi.org/10.1016/j.applthermaleng.2023.120100.

[18] Thakur, S.S., Akula, R., Kumar, L., 2024, An effective and lightweight battery thermal management system with incremental contact area: A numerical study. Applied Thermal Engineering, 242, 122555. doi: https://doi.org/10.1016/j.applthermaleng.2024.122555.

[19] Shan, S., Li, L., Xu, Q., Ling, L., Xie, Y., Wang, H., Zheng, K., Zhang, L., Bei, S., 2023. Numerical investigation of a compact and lightweight thermal management system with axially mounted cooling tubes for cylindrical lithium-ion battery module. Energy, 274, 127410. doi: https://doi.org/10.1016/j.energy.2023.127410.

[20] Yates, M., Akrami, M., Javadi, A.A., 2021, Analysing the performance of liquid cooling designs in cylindrical lithium-ion batteries. Journal of Energy Storage, 33, 100913. doi: https://doi.org/10.1016/j.est.2019.100913.

[21] Rao, Z., Qian, Z., Kuang, Y., Li, Y., 2017. Thermal performance of liquid cooling based thermal management system for cylindrical lithium-ion battery module with variable contact surface. Applied Thermal Engineering, 123, pp. 1514-1522. doi: https://doi.org/10.1016/j.applthermaleng.2017.06.059.

[22] White, F., 2005. Viscous Fluid Flow, (3rd edition), McGraw-Hill.

[23] Huang, H., Wang, H., Gu, J., Wu, Y., 2019. High-dimensional model representation-based global sensitivity analysis and the design of a novel thermal management system for lithium-ion batteries. Energy Conversion and Management, 190, pp. 54-72. doi: https://doi.org/10.1016/j.enconman.2019.04.013.

[24] Sutheesh, P.M., Nichit, R.B., Rohinikumar, B., 2024. Numerical investigation of thermal management of lithium ion battery pack with nano-enhanced phase change material and heat pipe. Journal of Energy Storage, 77, 109972. doi: https://doi.org/10.1016/j.est.2023.109972

[25] Jiaqiang, E., Yue, M., Chen, J., Zhu, H., Deng, Y., Zhu, Y., Zhang, F., Wen, M., Zhang, B., Kang, S., 2018. Effects of the different air cooling strategies on cooling performance of a lithium-ion battery module with baffle. Applied Thermal Engineering, 144, pp. 231-241. doi: https://doi.org/10.1016/j.applthermaleng.2018.08.064.

[26] Mubashir, M., Xu, J., Guo, Z., Wang, X., Wang, H., Qiao, F., Li, E., Mei, X., 2024. Numerical investigation of a novel cold plate design with uniform circular hollow fins for battery thermal management systems. Applied Thermal Engineering, 237, 121791. doi:

https://doi.org/10.1016/j.applthermaleng.2023.121791.

[27] Azmi, W.H., Sharma, K.V., Mamat, R., Alias, A.B.S., Misnon, I.I., 2012. Correlations for thermal conductivity and viscosity of water based nanofluids. IOP Conference Series: Materials Science and Engineering, 36, 012029. doi: 10.1088/1757-899X/36/1/012029.

[28] Sarvar-Ardeh, S., Rafee, R., Rashidi, S., 2022. Effects of convergence and superhydrophobicity on the hydrothermal features of the tapered double-layer microchannel. International Journal of Thermal Sciences, 181, p.107745.

[29] Bejan, A., 2013. Convection heat transfer, Fourth Edition, John wiley & sons, New York.

[30] Sarvar-Ardeh, S., Rafee, R., Rashidi, S., 2023. Heat transfer and entropy generation of hybrid nanofluid inside the convergent double-layer tapered microchannel, Mathematical Methods in the Applied Sciences, 46, pp. 11618-11641. doi: https://doi.org/10.1002/mma.8286.

[31] Sarvar-Ardeh, S., Rafee, R., Rashidi, S., 2023. Enhancing the performance of liquid-based battery thermal management system by porous substrate minichannel. Journal of Energy Storage, 71, 108142. doi: https://doi.org/10.1016/j.est.2023.108142.